



Determination of the porosity and its heterogeneity of fuel cell microporous layers by X-ray tomographic microscopy

Yen-Chun Chen^a, Chrysoula Karageorgiou^a, Jens Eller^a, Thomas J. Schmidt^{a,b}, Felix N. Büchi^{a,*}

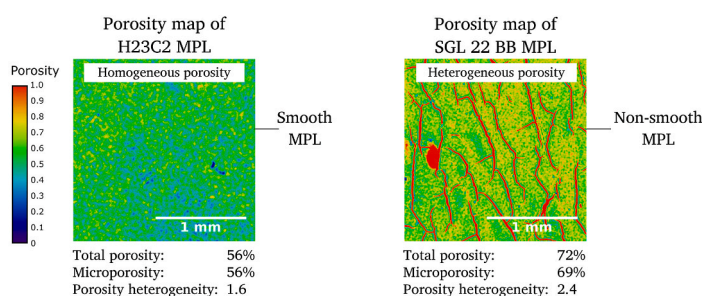
^a Electrochemistry Laboratory, Paul Scherrer Institut, 5232, Villigen PSI, Switzerland

^b Laboratory of Physical Chemistry, ETH Zürich, 8093, Zürich, Switzerland

HIGHLIGHTS

- Porosity and morphology of microporous layers (MPLs) are highly diverse.
- MPL total and micro-porosity from 15 commonly used gas diffusion layers are given.
- MPLs are categorized into five groups based on porosity and thickness heterogeneity.
- Homogeneous, smooth assumptions of MPLs do not always hold for all MPLs.
- Data for commonly used MPLs are provided for realistic modeling input values.

GRAPHICAL ABSTRACT



ARTICLE INFO

Keywords:

Microporous layer porosity
Heterogeneous porosity
Microporous layer morphology
Gradient porosity
Polymer electrolyte fuel cell

ABSTRACT

Advancing polymer electrolyte fuel cell technology includes the rational design of the microporous layer (MPL) coating on the gas diffusion layer (GDL), where the porosity and morphology on an operation-relevant size scale are still largely undetermined and hinder further developments. Here, 15 commercially available GDLs with MPL coatings from three major manufacturers (seven Freudenberg, four Sigracet® SGL and four CeTech materials) were characterized by X-ray tomographic microscopy. An extensive set of structural parameters for the MPLs are presented, including MPL total porosity, microporosity, porosity heterogeneity and thickness heterogeneity. The analyses show that the CeTech GDLs tend to have MPLs with the lowest porosity, while the Sigracet® GDLs have MPL with the highest porosity. Furthermore, Freudenberg H23 materials have the lowest porosity heterogeneity, and the Freudenberg CX materials' porosity are most heterogeneous. Many of the commercial MPLs, expected to be homogeneous, show a gradient of MPL microporosity in the thickness direction. The characterized MPLs are classified into five distinct classes based on thickness and porosity heterogeneities. This classification and the detailed data presented support the understanding of fuel cell performances with different MPL types. The comprehensive set of data also serve as realistic input values for material and fuel cell modeling studies.

* Corresponding author.

E-mail address: felix.buechi@psi.ch (F.N. Büchi).

<https://doi.org/10.1016/j.jpowsour.2022.231612>

Received 9 March 2022; Received in revised form 4 May 2022; Accepted 9 May 2022

Available online 20 May 2022

0378-7753/© 2022 The Authors. Published by Elsevier B.V. This is an open access article under the CC BY-NC-ND license (<http://creativecommons.org/licenses/by-nc-nd/4.0/>).

1. Introduction

Polymer electrolyte fuel cells (PEFCs) will be an integral part of future clean energy systems based on green hydrogen. In mobility sectors, the clean and low emission aspects of fuel cell electric vehicles provide an attractive alternative to the current transportation scheme, and hydrogen is a resilient energy vector that enables long-term energy storage solutions [1].

In the development of PEFCs, one of the bottlenecks is the water management. A delicate balance between maintaining an ion-conductive polymer electrolyte and preventing water flooding in the porous structures is necessary for operating PEFCs durably and efficiently. To enhance PEFC performance, the application of microporous layers (MPLs) on the gas diffusion layers (GDLs) and its advanced structural engineering are a common practice [2,3].

Commonly used microporous layers (MPL) consist of carbon or graphite nanoparticles and fluoropolymer binders (e.g. PTFE or FEP) that maintain the pore structure while granting a hydrophobic surface property [4]. The common pore size of MPLs is within the range of 20–500 nm [5], magnitudes lower than the some of the gas diffusion layers (GDLs). It has been repetitively shown that the addition of MPLs improves PEFC performance, especially water management [6–13]. The mechanisms that improve fuel cell performance are not completely understood so far. However, a few hypotheses and observations are consistently made. For example, MPLs may prevent the water in the GDL from building up at the surface of the catalyst layer and blocking reaction sites [5,12,14–17]. MPLs also reduce the water saturation in the GDL during operation due to the proposed reduction of water entry points from the catalyst layer (CL) to the GDL [2,12,18,19]. This should effectively lower the mass transport overpotential and, consequently, improve PEFC performance. Due to the smaller pore size of MPLs, the gradient in capillary force across the transport layers for liquid water is said to provide effective wicking that facilitates water drainage [4,13]. Yet, some think that the capillary barrier may rather compel liquid water generated at the cathode to permeate towards the anode. This process should promote membrane hydration [7,20–23]. In the late decade, structural modification of MPLs has received growing attention, as it was shown that the pore size distribution (PSD), thickness, surface wettability [24] and manufacturing processes [25] can all have influences on controlling PEFC performance. But, as the PEFC performance improvement by MPLs is generally highly dependent on the exact PEFC operation conditions, conflicting reports are unexceptional [2,11,26–29].

A variety of commercially available MPLs have pronounced crack features on its surface [30]. These cracks are believed to provide liquid water pathways for fast water transport or improve PEFC performance [26,27,31–34]. Yet even the exact role of cracks is not fully clear, because it again depends on the operation conditions of PEFCs and there are also reports stating that cracks in MPLs result in worse performance [35–37]. Owejan et al. hinted that cracks may not be necessary when most of the water transport in the MPLs would take place in gaseous form [14]. Alrwashdeh et al. later noted that cell temperature, rather than MPL cracks, is the predetermining factor in accounting for the water transport [38], consistent with the finding of a few studies [39,40]. Notably, there is also a non-negligible share of the market constituted by smooth (crack-free) MPLs, suggesting that the choice of MPL structures indeed depends on the operation conditions.

Among the MPL properties that determine water management efficiency, porosity is influential and has been challenging to determine in situ especially on a size scale relevant to fuel cell operations ($\gg 2 \text{ mm}^2$ in area [41]). Commonly it is determined in a bulk volume by mercury intrusion porosimetry (MIP) or a small volume by focused ion beam scanning electron microscopy (FIBSEM) [11,26,28,34,42–48] that may not be representative to the whole MPL area and does not give information on the lateral inhomogeneity. As a result, from time to time, homogeneous porosity for the whole MPL or an approximation to the

MPL porosity is assumed [49–52]. Furthermore, as gradient porosity design has been shown to be beneficial [11,53,54] and the importance of porosity and PSD is more recognized [26,28,55], it becomes crucial to characterize and quantify porosity heterogeneity of MPLs over a representative volume to promote understanding.

Unlike for GDLs, the explicit porosity values for the MPLs are often unavailable. Muirhead et al. and Banerjee et al. probed the through-plane porosity variation of SGL 25 BC and SGL 29 BC MPLs by X-ray tomographic microscopy (XTM), assuming constant MPL microporosity of 50% [50,51]. Accounting for the crack, this gives microporosity values of 60% and $\sim 55\%$ for SGL 25 BC and SGL 29 BC for the MPL domain, respectively. However, Antolini et al. pointed out that microporosity (pore size 3.8–350 nm) varies depending on the concentration of PTFE in the MPL. Therefore, a constant microporosity assumption for different MPLs might incur noticeable error from the actual porosity of the MPLs. In fact, when Alrwashdeh et al. derived the water saturation in the MPL with operando XTM imaging, they assumed a single value of 60% porosity for the SGL 28 BC gas diffusion layer, which led to saturation values higher than 1 in their estimations. This shows that the homogeneous porosity assumption was erroneous [49]. A recent study from the authors of this manuscript demonstrated that the MPL porosity has local variation even for the Freudenberg H23C6 GDL, which comes with a smooth, crack-free MPL coating. The H23C6 MPL in-plane porosity fluctuates up to $\pm 10\%$ [56]. This is larger than some gradient porosity MPL designs having $<10\%$ porosity difference [53]. The implication is that either the local porosity difference in a MPL is larger than some of the gradient-porosity MPLs, or the homogeneous assumption of MPL porosity will lead to significant error in saturation estimation.

Until now, there still lacks accurate data of the porosity values and related structural parameters of MPLs that affect PEFC water transport mechanisms. Often researchers rely on the values given by the manufacturer or need to make assumptions for the properties (such as porosity) that are not straightforward to obtain.

In this work, we use a laboratory computed tomography (lab-CT) scanner in a quantitative manner to characterize 15 MPLs from three commercial GDL manufacturers (Freudenberg, SGL, CeTech). The XTM method allows to accurately determine the MPL porosity and the three-dimensional spatial distribution of porosity heterogeneity, as previously described [56], and to analyze the morphology (cracks, thickness, MPL/GDL volume ratio, etc.) of the different MPL materials. MPLs are thus classified into five classes defined by porosity and thickness homogeneity. The results are expected to provide insight for future studies using the different commercial MPLs to better understand the PEFC performances at the diffusion layers' level. The reported physical properties and morphology descriptions are directly obtained from quantitative imaging without MPL property assumptions, and thus provide a better estimation for the MPL thickness, porosity and their heterogeneity.

2. Experimental section

2.1. Materials

2.1.1. Commercial MPLs

Seven Freudenberg GDLs with MPLs (H23C2, H23C4, H23C6, H23C9, H23C10, H14CX653, H24CX483), four Sigracet® GDLs with MPLs (SGL 22 BB, SGL 25 BC, SGL 28 BC, SGL 36 BB) and four CeTech GDLs with MPLs (CT W1S1009, CT W1S1010, CT GDL 120S, CT GDL 210S) were characterized. All GDLs were purchased from The Fuel Cell Store (Texas 77845, USA).

2.1.2. Liquids

N-decane (Thermo Fisher/Fisher Scientific AG, Switzerland) was used to achieve complete saturation of MPLs. Ethanol absolute ($\geq 99.8\%$) used for greyscale value calibration was purchased from

Merck KGaA, Germany. Deionized water ($380 \pm 50 \text{ k}\Omega \text{ cm}$) was used wherever water is mentioned.

2.1.3. PEEK cylindrical sample holder

A low X-ray absorbing, tubular sample holder made of polyether-ether-ketone (PEEK) with an inner chamber of 7.5 mm diameter and outer diameter 10 mm for material housing was used for X-ray tomographic image acquisition. The design has been presented in detail previously, [56] and can be found in the Supplementary Materials (Fig. S1). To fix the sample, an adjustable compression screw and a closing piece clamp the samples vertically. The chamber has a fixed floor with an open injection hole, which allows liquids to be injected from the bottom into the chamber, while the air leaves from the top of the chamber through the hole in the closing piece. A syringe pump (Fisher Scientific) with connected tubing (Festo, type: PUN-H-3 \times 0.5 NT) was used to inject liquid during the wetting procedure.

2.2. XTM acquisition parameters

A computed tomography (CT) scanner, Phoenix nanotom m (General Electric, Germany), with a Phoenix|X-ray micro-focus tube was used to obtain all tomographic data. Acquisition parameters that lead to quantitative images were used to ensure data comparability: X-ray tube acceleration voltage was set to 80 kV and current to 280 μA . The exposure time for each radiographic projection was 1.5 s for all the materials. Every three consecutive projections were averaged to produce one image for later reconstruction. A total of 2400 images (for all the materials) were obtained for tomographic reconstruction. During the scans, all scanned objects including the sample holder were completely within the detector field of view to avoid local tomography—an essential step to make sure that the (32-bit floating point) greyscale values are comparable across scans. Flat field correction was done before every scan and a radiographic region of constant air phase was chosen as the “observational ROI” to compensate X-ray intensity fluctuations during the CT scans and improve image quantifiability. The voxel edge length was 3.6 μm and the total acquisition time was 3 h per tomographic scan.

2.3. Derivation of MPL porosity by XTM

2.3.1. XTM greyscale value calibration

Tomography with polychromatic X-ray sources requires greyscale value (GSV) calibration with materials of known linear attenuation coefficients to achieve quantitative imaging. The method was described in detail before [56]. Briefly, MPL-composing materials such as air, pyrolytic graphite (Union Carbide, USA) and PTFE—plus associated materials in the experiments: n-decane, ethanol absolute, PEEK and water—were imaged and their GSVs were compared to their linear attenuation coefficients (NIST database [57,58]). With a MATLAB script whose working principle was described elsewhere [56], it was confirmed that a linear correlation exists between the tomographic GSVs and the linear attenuation coefficients at X-ray energy 32.09 keV with an R^2 value of 0.997 (Fig. S2, Supplementary Materials).

The highly linear relationship shows that the mass density of water, n-decane and ethanol in the MPL (consisting of graphite, air and PTFE) pores can be analyzed and determined from the imaged greyscale values (GSVs). Their GSVs and linear attenuation coefficients can be approximately described by the linear function:

$$GSV(\vec{r}, E_1) = \sum_i^n C_1 \mu_i(\rho, V, Z, \vec{r}, E_2, 32.09 \text{ keV}) + C_2 \quad (1)$$

where \vec{r} denotes the voxel position; E_1 is the energy distribution of the X-ray from the X-ray tube; i represents the material phase (i.e., air, n-decane, ethanol, etc.); μ_i denotes the linear attenuation coefficient of the i th material phase. ρ , V , Z and E_2 are written explicitly to express the dependence of the linear attenuation coefficients on the density,

volume, atomic number and photon energy associated with the material phases. C_1 and C_2 are constants and in the specific case of using the aforementioned tomographic acquisition parameters with X-ray tube acceleration voltage 80 kV and current 280 μA , C_1 and C_2 are 0.104 and 0.00177.

2.3.2. MPL porosity determination from XTM images

MPLs (on their respective GDL substrates) were first scanned at dry condition (dry image). Then the MPLs were fully saturated by injecting an excessive amount of a wetting liquid, n-decane, in the sample chamber. Any remaining air in the MPL pores was removed by evacuation at $<5 \text{ mbar}$ for $>90 \text{ min}$ at room temperature (RT). After aligning the wet image against the dry image using 3Dslicer [59] (rigid and affine registration), the difference of GSVs in the wet and dry images was calculated by ImageJ. The resulting image is referred to as the “difference image”. In the difference image, since the only change is the n-decane filling, the greyscale value at each voxel ($GSV_{\text{diff img}}(\vec{r})$) is directly proportional to the n-decane mass at that voxel. Under isothermic experimental conditions, the $GSV_{\text{diff img}}$ is thus proportional to the MPL open porosity (ϵ) at each voxel due to full saturation:

$$GSV_{\text{diff img}}(\vec{r}) \propto \mu_{n\text{-decane}}(\vec{r}) \propto \mu_{\text{mass, n-decane}} \cdot P_{n\text{-decane}}(\vec{r}) \propto M_{n\text{-decane}}(\vec{r}) \quad (2)$$

$$GSV_{\text{diff img}}(\vec{r}) \propto \dot{V}_{n\text{-decane}}(\vec{r}) \text{ (isothermic condition)} \quad (3)$$

$$GSV_{\text{diff img}}(\vec{r}) \propto \epsilon(\vec{r}) \text{ (fully saturated MPLs)} \quad (4)$$

where $\mu_{n\text{-decane}}$ is the linear attenuation coefficient of n-decane; $\mu_{\text{mass, n-decane}}$, $P_{n\text{-decane}}(\vec{r})$, $M_{n\text{-decane}}$ and $\dot{V}_{n\text{-decane}}$ are the mass attenuation coefficient of n-decane, mass density of n-decane with respect to the voxel (at \vec{r}) and the voxel volume fraction occupied by n-decane.

When normalized against the average GSV of the free-standing n-decane pool or droplets (100% n-decane volume fraction) close to the sample, the difference image shows the MPL porosity spatial distribution in three dimensions.

2.4. Image processing

2.4.1. MPL segmentation, crack volume ratio, thickness map and microporosity

The tomographic images are raw 32-bit dry images. Before segmenting the MPL and the GDL phases, a median filter of 1.5 pixel radius was applied to the image to remove noise signals while preserving the MPL crack structure. The images were transformed to 8-bit and an edge-preserving bilateral filter (ImageJ process) was subsequently applied with spatial radius = 3 and range radius = 15 to separate the fiber, MPL and void (including crack) phases. Then thresholding of the MPL phase was based on manually selected threshold values for each image stack and the results were carefully reviewed across the whole GDL stack to get reliable binary images of MPLs. The segmented binary images of the MPLs were directly used to derive MPL crack volume percentage with respect to the total MPL volume (including crack volume).

To obtain accurate MPL thickness maps, ImageJ process “erode” was carried out once on the segmented binary images of the MPLs to remove the voxels from GDL fibers that were not eliminated during the manual segmentation step. The erosion process was done for four to six times to determine MPL microporosity reliably without edge enhancement artifact influence.

2.5. MPL porosity maps

The difference images (wet minus dry) were normalized against $GSV_{n\text{-decane}}$ to obtain the MPL porosity distribution. The resultant image is still affected by X-ray quantum noise. Since this random noise is approximately Poisson and can be approximated by a Gaussian

distribution at large sampling numbers, isotropic 2D mean filtering was chosen to reduce the image noise. Additionally, there is a straightforward relationship between the (Gaussian) noise reduction efficiency and voxel averaging that makes the mean filter beneficial, as each mean filter kernel size corresponds to a certain area over which the image is averaged. A radius of three voxels for all the materials were determined to be the best compromise in reducing image noise while preserving small image features. ImageJ LUT “physics” was applied to the filtered, normalized difference images to render color-coded MPL porosity maps. An error bar describing the random noise, which was evaluated by measuring the standard deviation of the GSVs of the n-decane pool nearby the MPL tomographic slices, is added to the porosity maps. In the n-decane pools or droplets, the X-ray attenuation is constant. Therefore, the standard deviation in GSV there (σ) is a direct estimation of the standard deviation of the porosity evaluation of each voxel in the tomographic image.

2.6. MPL/GDL porosity profiles

Through-plane porosity profiles are given for some GDL samples to elucidate the porosity variation in the thickness direction. Both the MPL and the GDL substrate domains were characterized. In the MPL domain, difference images were used to provide MPL porosity. In the GDL domain, dominated by fibers and void space, the binary segmented images were used to evaluate GDL substrate porosity. At the interfacial region where fiber, MPL and void phases co-exist, phases were separated and their area percentage measured. The porosity is estimated from the void and MPL area percentage, assigning the MPL phase with the average microporosity value measured from the MPL bulk (a measure to mitigate the potential MPL porosity estimation error from under-sampling effect at the MPL/GDL interfacial region due to reduced MPL voxels). Due to the different methods used for evaluating the porosity values across the morphologically distinct diffusion layers, minor discontinuity occurs sometimes at the MPL/GDL interfacial region.

2.7. MPL porosity discernability by XTM

Unlike tomographic image processing by segmentation, when evaluating the porosity from the GSVs (in difference images), image noise is an important factor to consider. Every voxel is influenced by uncertainty from X-ray noise.

The uncertainty is approximated by a Gaussian function. It is derived that if two regions of MPLs have the same actual physical porosity, then there is a 95% chance that their imaged porosity will not differ by $\geq 2.8\sigma$, where σ is the standard error (see section 2.5) in porosity evaluation (details in **Supplementary Materials** section 3 and Fig. S3). In other words, a porosity difference $\geq 2.8\sigma$ is the criterion to judge (with 95% confidence level) that two regions have different physical porosity. Furthermore, when multiple voxels are averaged and compared—this is equivalent to comparing the area-averaged porosity values of different MPL regions—the standard error decreases with respect to the inverse square root of the voxel number N ($\sigma \propto N^{-0.5}$) in the case of no image artifacts. The larger the MPL area over which the average porosity is taken, the more voxels are averaged, thus the lower the standard error and the more precise the porosity reading. For porosity images (also addressed as “porosity maps”) scanned for 3 h and mean-filtered with a radius of 3 voxels, the discernability curve is experimentally measured with respect to the area of MPL over which the average porosity is taken. It is summarized in Fig. S4 in the **Supplementary Materials**.

The discernability curve in Fig. S4 follows the $\sigma \propto N^{-0.5}$ relationship. Therefore, the standard error is a result of quantum mottle in the measured area in the tomographic image and image artifacts are negligible. For some images, the exponent is larger (typically about -0.3 to -0.4), which indicates the existence of imaging artifacts (from X-ray intensity fluctuation, beam hardening etc.) Nevertheless, with scrutiny,

the discernability curve can still be applied to those images where there is no distinct phase boundaries (to avoid edge enhancement), because the discernability curve also takes into account small deviations caused by imaging artifacts other than edge enhancement.

The high image quality of 3 h scans results in a good 2.8σ discernability of 12.7% for **single voxel** porosity comparisons. Between every voxel (edge length = $3.6 \mu\text{m}$) in the porosity map, a difference of $\geq 12.7\%$ was sufficient to judge (with 95% confidence level) that the MPL had different physical porosity at these measured voxel locations. For most results reported, the average porosity of regions having $50 \mu\text{m} \times 50 \mu\text{m}$ ($= 2500 \mu\text{m}^2$) area across the MPL were compared; the corresponding discernability of 4.7% then means that the area-averaged porosity can be discerned from noise once the difference is $\geq 4.7\%$ (Fig. S4). The XTM method is thus a highly sensitive tool for heterogeneous MPL porosity evaluation over a length scale of several millimeters.

2.8. Thickness, thickness heterogeneity and areal porosity heterogeneity

The apparent thickness is how thick the MPL “looks” when seen from the side (through-plane cross-section), and is defined to be the FWHM (full width at half maximum) of the peak shape when the MPL area percentage is plotted against the through-plane distance (details **Supplementary Materials**, Fig. S5). The effective thickness is the total MPL volume (excluding MPL cracks and holes) divided by the area the MPL covers, which reflects how much MPL materials are used on a gas diffusion layer.

Some MPLs have higher local thickness variation. To quantify the heterogeneity of MPL thickness, the MPL thickness maps are first obtained by segmentation and summing up the MPL voxels (edge length = $3.6 \mu\text{m}$) in the thickness direction. The standard deviation of the thickness values across the whole inspected MPL area ($12\text{--}28 \text{ mm}^2$ for all samples) is subsequently defined to be the thickness heterogeneity.

A straightforward way to quantify the MPL porosity heterogeneity is to compare the standard deviation of the MPL porosity ($\sigma_{\text{MPL porosity}}$) in the porosity images to the standard deviation of the n-decane pool in the same image ($\sigma_{\text{n-decane}}$). Assuming negligible image artifacts, the former ($\sigma_{\text{MPL porosity}}$) is a result of both the MPL spatial porosity variation and the X-ray noise, while the latter is solely a reflection of the X-ray noise. The quotient of the two standard deviation values then reveals the extent to which the MPL porosity varies across the MPL area. Since in practice the (porosity) heterogeneity is measured for each two-dimensional areal slice, it is also termed:

$$(\text{Areal}) \text{ porosity heterogeneity} = \frac{\sigma_{\text{MPL porosity}}}{\sigma_{\text{n-decane}}} \quad (5)$$

When the MPL porosity distribution would be completely homogeneous, the (areal) porosity heterogeneity would be unity, meaning that the MPL spatial porosity distribution is as “even” as the n-decane pool (porosity being perfectly the same “100%” everywhere).

To reduce the contribution from X-ray noise to the standard deviations, the porosity maps are binned in such a way that voxel-to-voxel error is reduced to ca. 4.5% or lower prior to standard deviation calculation. Binning size is therefore 14 by 14 for all samples. This means, the porosity heterogeneity is evaluated on a scale of ca. $50 \mu\text{m}$ when using the binned areas of ca. $50 \times 50 \mu\text{m}^2$.

2.9. Representativeness of the data

All structural properties (total porosity, microporosity, thickness, crack volume ratio, MPL volume ratio and porosity and thickness heterogeneity) were derived from XTM images of GDLs cut in circular disks of diameter 4–6 mm. Consequently, image stacks with $12.6\text{--}28.3 \text{ mm}^2$ area per slice and 3–15 slices were available and used for data analyses. Therefore, the analyzed MPL volumes are in the range of $0.14\text{--}1.5 \text{ mm}^3$. It is a much larger volume compared to typical FIBSEM field of view (usually $<0.001 \text{ mm}^3$ volume coverage).

The analyzed area is 3–4 orders of magnitude larger than the average pore cross section of the paper GDL substrates [60] and the characterized GDL length scale is still about one order of magnitude larger than the repetitive features of the woven substrates.

To ensure that the MPL data are representative, at least two different GDL samples from each commercial provider were scanned after sampling them at two separate positions at least 2 cm apart on the GDL sheets. The results for MPLs were averaged. All the GDL sheets inspected at two separate positions showed high consistency of the MPL porosity values (within average porosity $\pm 4.5\%$). It is thus concluded that the imaged samples are large enough to be representative of the MPLs, and the structural properties derived here are able to describe the MPLs of the commercial GDL products.

The representativeness of the substrate porosity profiles is enhanced by ensuring that all porosity profile characterizations are based on averaged results of in-plane area $>12 \text{ mm}^2$ at each through-plane position.

3. Results and discussion

Gas diffusion layers with MPL coatings from three different international manufacturers, Freudenberg, Sigracet® and CeTech, are selected and characterized due to the worldwide adoption of these materials. Also, as the substrate GDLs influences the MPL morphology, the three frequently used substrate types are represented: Freudenberg (dry-laid water-jet-entangled), Sigracet (wet-laid with binder) and CeTech (woven substrate). Since the MPLs from the same manufacturer have comparable morphology and porosity, the results are grouped according to the manufacturers.

The total porosity (porosity including cracks) and microporosity (porosity without cracks) of the MPLs are characterized separately. As a novelty, the MPL porosity heterogeneity accounting for the crack structure and microporosity variation is analyzed and described by the quantitative parameter, porosity heterogeneity (Experimental section 2.8), which indicates how disperse the spatial porosity distribution is.

For the representativeness of the characterization, at least two samples of each gas diffusion layers from each manufacturer group are analyzed at two random, separate positions on the GDL sheet and the results are found to be highly consistent. Details on representativeness can be found in the Experimental section 2.9.

Table 1

MPL structural properties: total porosity includes MPLs material porosity and crack volume; microporosity is the MPL material porosity (from sub-micrometer scale pores); (areal) porosity heterogeneity is determined on 50 μm -scale (exact definition see Experimental section 2.8); effective thickness is the total MPL volume divided by the geometric area; apparent thickness is the FWHM of the MPL area percentage plot versus through-plane distance; thickness heterogeneity is defined by the thickness standard deviation measured from the thickness maps (Experimental section 2.8).

GDL manufacturer	GDL name	Average MPL total porosity	Average MPL micro-porosity	(Areal) porosity heterogeneity	Effective MPL thickness (μm)	Apparent MPL thickness (μm)	Thickness heterogeneity (μm)	GDL thickness including MPL (μm)	MPL volume ratio	Average crack volume%
Freudenberg	H23C2	$56 \pm 3\%$	$= 56 \pm 3\%$	1.6 ± 0.2	41	43	8	209	20%	$<1\%$
	H23C4	60%	$= 60\%$	1.7 ± 0.2	46	50	8	234	20%	$<1\%$
	H23C6	$61 \pm 0\%$	$= 61 \pm 0\%$	2.1 ± 0.2	30	36	6	212	14%	$<1\%$
	H23C9	60%	$= 60\%$	1.7 ± 0.2	32	34	7	209	15%	$<1\%$
	H23C10	$56 \pm 3\%$	$= 56 \pm 3\%$	1.6 ± 0.2	32	34	8	205	16%	$<1\%$
	H14CX653	$66 \pm 4\%$	N/A	3.7 ± 0.5	34	38	4*	158	22%	N/A
	H24CX483	68%	N/A	6.1 ± 0.4	27	32	5*	223	12%	N/A
Sigracet	SGL 22 BB	$72 \pm 2\%$	$69 \pm 3\%$	2.4 ± 0.3	55	71	22	199	28%	8.7%
	SGL 25 BC	$70 \pm 2\%$	$69 \pm 3\%$	2.5 ± 0.5	63	68	28	223	40%	4.8%
	SGL 28 BC	$76 \pm 0\%$	$73 \pm 1\%$	2.9 ± 0.7	109	134	35	242	45%	7.8%
	SGL 36 BB	$75 \pm 2\%$	$73 \pm 1\%$	2.1 ± 0.3	68	83	27	270	26%	7.6%
CeTech	W1S1009	54%	48%	3.4 ± 0.9	60	72	30	353	17%	7.2%
	W1S1010	$54 \pm 3\%$	$46 \pm 4\%$	3.5 ± 0.6	45	81	30	342	13%	7.4%
	GDL120S	56%	51%	2.3 ± 0.1	36	43	12	130	28%	6.2%
	GDL210S	$62 \pm 1\%$	$55 \pm 3\%$	2.0 ± 0.2	23	28	9	197	12%	7.2%

1 N/A: not available because MPLs cannot be properly segmented.

3.1. Freudenberg H23 and CX materials

3.1.1. Tomographic images and porosity map interpretations

The Freudenberg H23CN (N = 2, 4, 6, 9, 10) GDLs are accompanied with MPLs $\leq 50 \mu\text{m}$ thick (apparent thickness), and the thickness heterogeneity is low (between 6 and 8 μm , Table 1). The MPLs have minor cracks that consist of $<1\%$ of the MPL volume. The cracks have ca. 10 μm width, and are short and isolated from one another. The total porosity (=microporosity due to the lack of cracks) of the H23 MPLs is 56–61%.

The Freudenberg CX GDLs' (H14CX653 and H24CX483) MPLs are 30–40 μm thick (apparent thickness) and have plenty of big openings with in-plane diameters in the range of ca. 20–70 μm aside from the nanoporous structures. Due to the distinct macropore structure, the crack volume ratio and microporosity of the CX GDLs is not defined here. The CX MPLs are more porous, with total porosity of 66–68%.

While the five materials of the H23 GDL series have similar thickness and porosity properties, the MPLs of H23C10 (most homogeneous) and H23C6 (least homogeneous) have different spatial porosity distributions. Their tomographic images and porosity maps are presented in Fig. 1. The in-plane tomographic slices show the somewhat different morphology of the two GDLs; H23C10 appears more homogeneous, while H23C6 has inhomogeneous local features appearing as white bands and brighter domains, most probably stemming from a different fluorocarbon formulation. The porosity analysis shows that H23C10 has an even porosity across the inspected region with an average total porosity of 56%, whereas H23C6 has somewhat more noticeable porosity variations over the same area at a slightly higher total porosity of 61%. The in-plane porosity heterogeneity—which describes the degree of spatial porosity variation—of H23C10 MPL is 1.6 ± 0.2 , and for H23C6 MPL it is 2.1 ± 0.2 . The through-plane porosity maps are provided to visualize the porosity values of MPLs in the through-plane direction. Porosity and porosity heterogeneity for the three other H23CN materials are listed in Table 1.

The 2.8 σ discernability criterion for the tomographic data (Fig. S4, Supplementary Materials) indicates that, examining each arbitrary 50 $\mu\text{m} \times 50 \mu\text{m}$ region in the in-plane porosity maps of Fig. 1, any area-averaged MPL porosity value differing $>4.7\%$ from one another can be judged to originate from physical porosity difference. This further proves that the porosity map of H23C6 shows physical porosity variations, not merely image noise.

The CX materials, H14CX653 MPL (average total porosity = 66%) and H24CX483 MPL (average total porosity = 68%), have both sub-

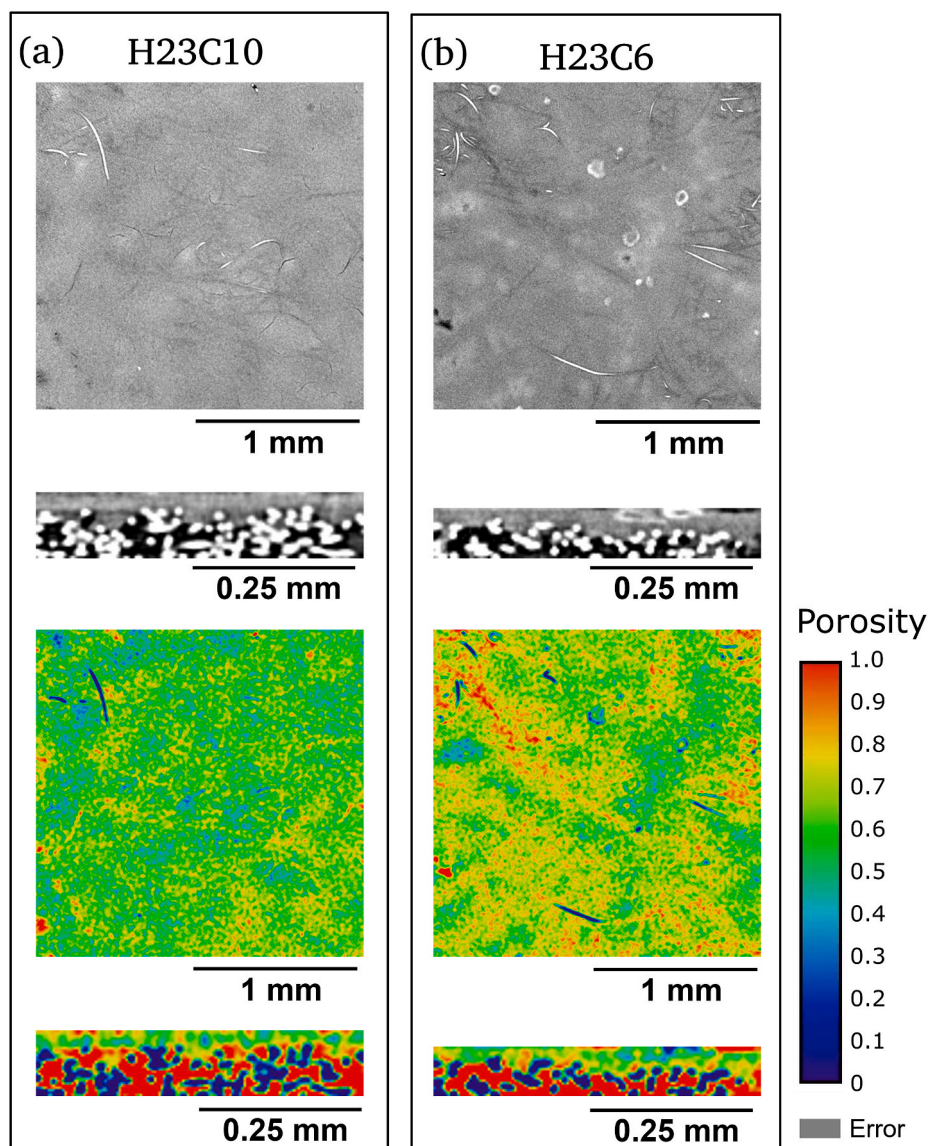


Fig. 1. Tomographic images and porosity maps of the MPLs of (a) Freudenberg H23C10 and (b) Freudenberg H23C6 GDLs; the in-plane and through-plane tomographic images and porosity maps are of the same respective positions. The error under the calibration bar denotes 1σ error for single-voxel porosity reading in the porosity maps.

micrometer- and micrometer-scale pores, which can be identified in Fig. 2. Bigger pores are resolved in the tomographic images, and have 100% local porosity, whereas the smaller sub-micron pores constitute regions with ca. 60% porosity in the porosity maps in Fig. 2a and b. Because of the large pores of the H24CX483 MPL, the underlying GDL substrate is exposed to the surface locally (Fig. 2b, through-plane images). Owing to the coexistence of the sub-micrometer- and micrometer-scale pores, CX MPLs' areal porosity heterogeneity is considerably higher (on the $50\ \mu\text{m} \times 50\ \mu\text{m}$ scale) than that of the H23 materials, at 3.7 ± 0.5 for H14CX653 and 6.1 ± 0.4 for H24CX483. The higher areal porosity heterogeneity of H24CX483 originates from the more dispersed pore size distribution, from 0% for the non-porous solid parts to 100% for the large pores up to ca. $70\ \mu\text{m}$ in diameter (Fig. 2b).

To aid the porosity map interpretation, a pure n-decane porosity map (porosity = 100%) whose fluctuation is purely a result of X-ray noise is provided to the right of Fig. 2b. The significantly higher heterogeneity in the CX materials' porosity maps proves that the variations seen in the porosity maps originate from the MPL physical porosity variations.

3.1.2. Porosity profiles

The (total) porosity profiles of the Freudenberg H23 and CX materials are provided in Fig. 3a, which shows the (in-plane-averaged) porosity with respect to the GDL depth, denoted as the through-plane distance. Here, $0\ \mu\text{m}$ through-plane distance designates the first slice close to the MPL surface that was analyzed. The schematic in Fig. 3b indicates the different zones of an MPL-coated GDL: MPL zone, MPL + GDL mixed zone and GDL substrate. Fig. 3b shows an example of an uneven MPL with high thickness heterogeneity.

CX MPLs generally have higher porosity (between 66 and 68%) than the H23 MPLs (56–61%) (Fig. 3a, MPL zone). There is also no porosity gradient within the MPL zone. However, many GDLs experience a decrease in porosity in the MPL + GDL mixed zone due to the fiber intrusion in the MPL. This is followed by an increase in porosity towards the GDL substrate because of the higher porosity of the GDL substrates. The porosity gradient from the MPL to GDL substrate is less for the CX materials than for H23 materials because the CX MPLs have higher porosity similar to that of the GDL substrates.

The total porosity, microporosity, thickness and porosity heterogeneity of the Freudenberg H23 and CX materials as well as MPLs from

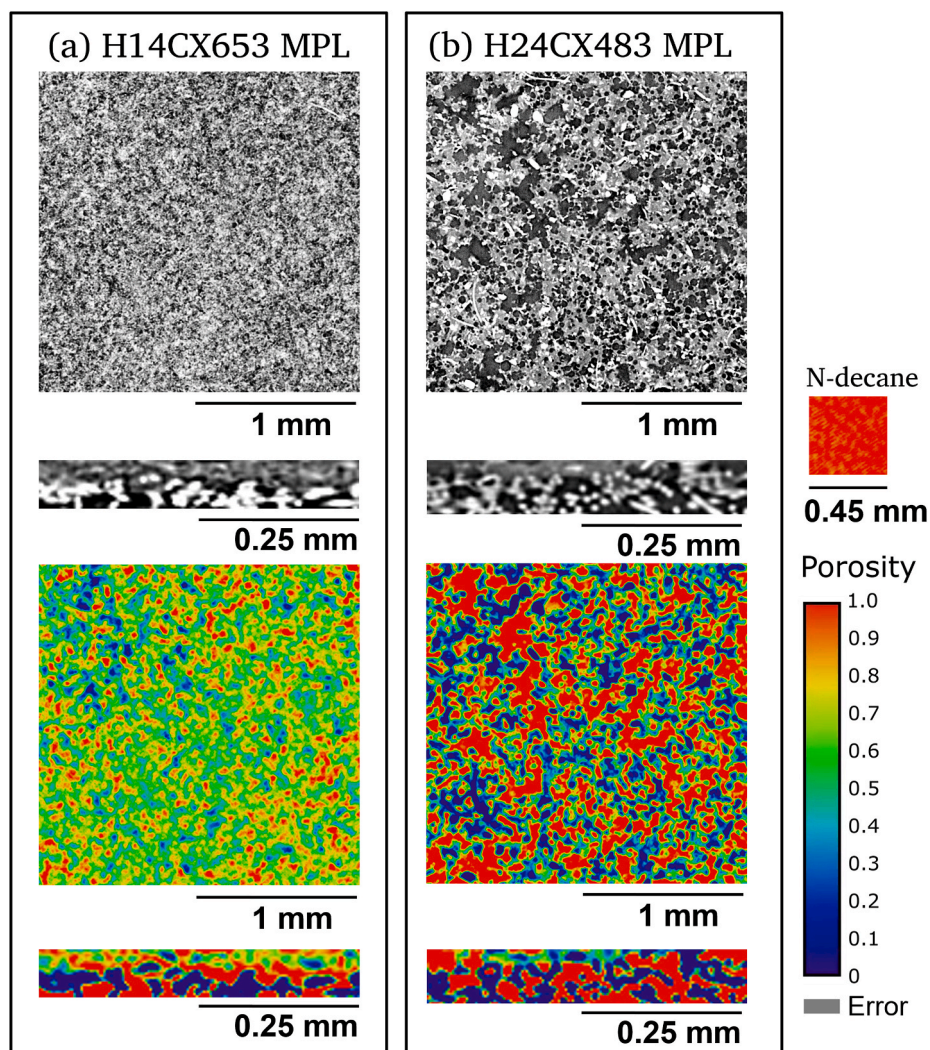


Fig. 2. Tomographic images and porosity maps of the MPLs of (a) Freudenberg H14CX653 and (b) Freudenberg H24CX 483 GDLs; the in-plane and through-plane tomographic images and porosity maps are of the same respective positions. The error under the calibration bar denotes 1σ error for single-voxel porosity reading in the porosity maps.

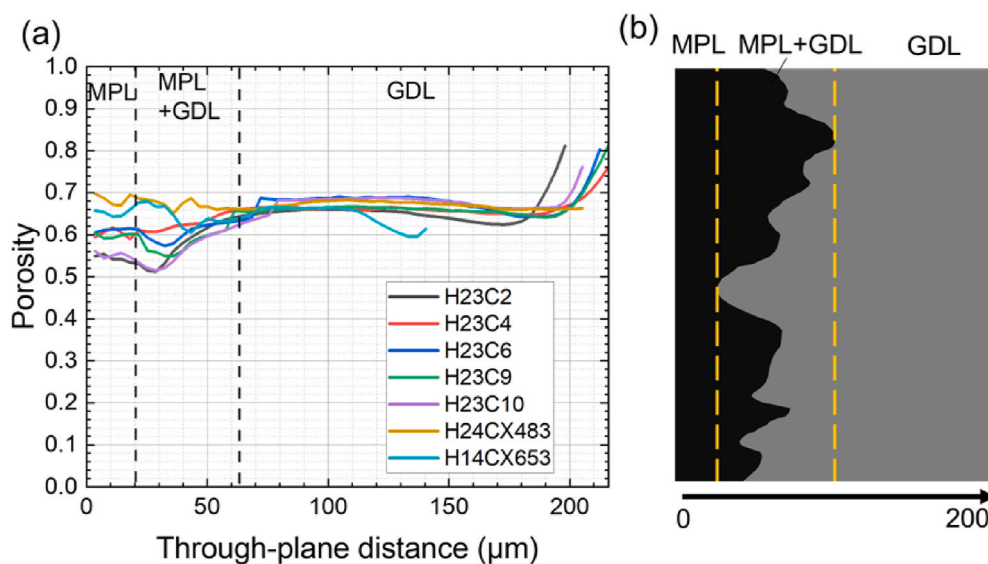


Fig. 3. (a) Porosity profiles of Freudenberg H23 and CX gas diffusion layers; through-plane distance starts from the first analyzed MPL surface slice; (b) schematic of a vertically placed GDL, aiding porosity profile interpretation and indicating different zones of an MPL-coated GDL.

other manufacturers are summarized in Table 1.

3.2. Sigracet® materials

3.2.1. Tomographic images and porosity map interpretations

The Sigracet® SGL 22BB, SGL 25 BC, SGL 28 BC and SGL 36 BB have MPLs with various average thickness (68–134 μm , apparent thickness). Furthermore, the MPL thickness heterogeneity is high (22–35 μm , Table 1); the thickness maps of Sigracet® materials together with all other MPLs' are provided in **Supplementary Materials, Figs. S6–8**, for visualization of the thickness heterogeneity. The cracks of the Sigracet® MPLs are pronounced and penetrating, constituting 4.8–8.7% of the total MPL volume. The total porosity of all (characterized) Sigracet®

materials is between 70% and 75%, and their microporosity also has a small range from 69% to 73%. All characterized Sigracet® materials have higher MPL microporosity than the Freudenberg materials.

The MPLs of SGL 28 BC and SGL 36 BB have different crack morphology and are compared in Fig. 4. SGL 28 BC has both holes and cracks in the MPL, but SGL 36 BB only has cracks and no holes are observed (Fig. 4a and b tomographic images). This is confirmed by examining two samples from different locations in the sheet. It is hypothesized that the thicker MPL of SGL 28 BC and potentially different sintering processes may be the reasons for the different MPL morphology. The through-plane images (Fig. 4a and b) show the features of the holes and the penetrating cracks of SGL 28 BC and SGL 36 BB MPLs, respectively, and suggest the highly heterogeneous MPL thickness

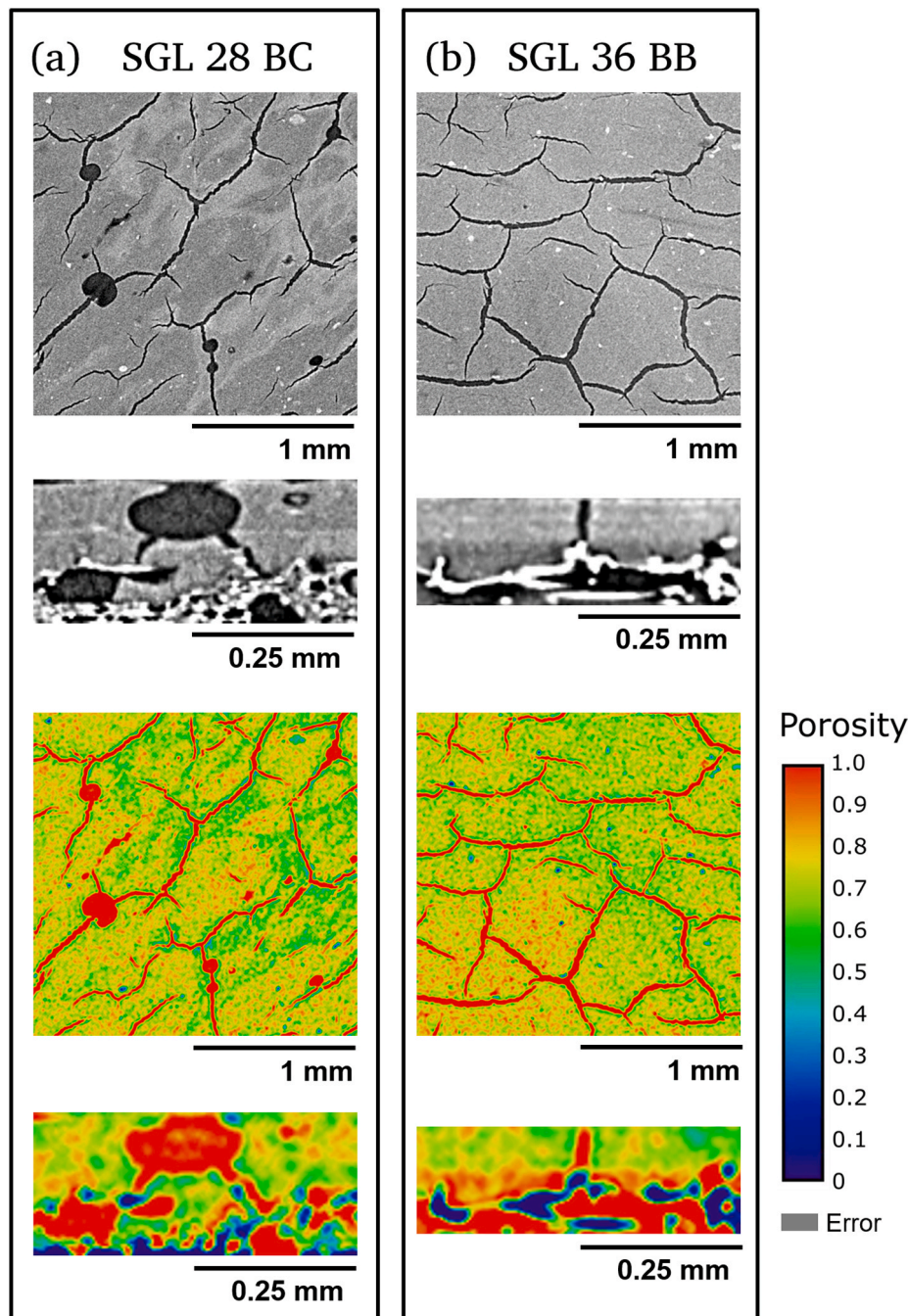


Fig. 4. Tomographic images and porosity maps of the MPLs of (a) Sigracet® SGL 28 BC and (b) SGL 36 BB GDLs; the in-plane and through-plane tomographic images and porosity maps are of the same respective positions. The error under the calibration bar denotes 1σ error for single-voxel porosity reading in the porosity maps.

distributions (additional MPL thickness maps provided in Fig. S7, Supplementary Materials). The through-plane porosity maps of the same positions are provided at the bottom of the figure.

The average total porosity of SGL 28 BC (76%) and SGL 36 BB (75%) MPLs are alike, because their MPL microporosity is the same (73%) and crack volume percentage similar (7.8% and 7.6%, see Table 1). Local porosity variations are observed for both MPLs, shown in the in-plane porosity maps of Fig. 4a and b. The distribution of porosity in the porosity maps do not suggest a regular pattern, and the crack structures contribute to increased porosity heterogeneity: 2.9 ± 0.7 and 2.1 ± 0.3 for SGL 28 BC and SGL 36 BB, respectively. The higher porosity heterogeneity of the former is a result of the additional contribution from the diverse hole structures.

The 2σ discernability criterion (Fig. S4) can be applied directly to interpret the porosity maps in Fig. 4. Comparing among $50 \mu\text{m} \times 50 \mu\text{m}$ -area regions, porosity difference $>4.7\%$ is a result of physical porosity difference (95% confidence level).

3.2.2. Porosity profiles

The microporosity and total porosity profiles of the Sigracet® GDLs are provided separately in Fig. 5.

All Sigracet® materials characterized have very similar microporosity profiles in the MPL zone (through-plane distance $\leq 50 \mu\text{m}$; this is only a rough estimation, because the MPLs have different thickness), with the surface region being denser (ca. 66–68% in porosity) than the deeper MPL-only material (72–74% in porosity) (Fig. 5a). This may be a consequence of the sintering process. Further into the MPL + GDL mixed zone, the microporosity starts to deviate, but remains vastly within the range of $72 \pm 10\%$. It is clear that the 50% or 60% microporosity assumption in previous studies for Sigracet® materials [49–51] was too low. Incidentally, due to the different thickness of the SGL GDLs, it is not possible to draw a line to discern the MPL + GDL mixed zone and the GDL zone for all SGL materials in one graph.

The total MPL porosity depends on the crack volume, and is naturally higher than the microporosity. SGL 28 BC has the highest porosity and SGL 25 BC the lowest (Fig. 5b), even though large-scale GDL substrate heterogeneity may not be captured with the present sample size. In general, the higher porosity of the Sigracet® MPLs is accountable for the lack of a porosity dip at the MPL/GDL interface as observed for the Freudenberg materials. Additionally, the existence of intruding MPLs has an impact on the GDL porosity in the MPL + GDL mixed zones, resulting in a lower total GDL porosity. Incidentally, the porosity dip at the GDL substrate bottom is likely a result of increasing binder phase (e.g. SGL 22 BB, through-plane distance 110–150 μm).

The total porosity, microporosity, thickness and porosity

heterogeneity of all Sigracet® materials are given in Table 1.

3.3. CeTech materials

3.3.1. Tomographic images and porosity map interpretations

Of the CeTech materials, CT W1S1009, CT W1S1010 are based on a woven substrate while GDL 120S and GDL 210S are carbon papers with binder. The MPLs come with average apparent thickness ranging from 28 to 81 μm and all have cracks taking up 6.2–7.4% of the MPL volume. The total porosity of the CeTech materials is in the range of 54–62% and thus the lowest range of the three investigated brands. Also, the microporosity of the MPLs, ranging from 46 to 55%, is the lowest among the different manufacturers compared here.

The morphology and porosity of MPL of a woven based (W1S1009) and a paper based material (GDL120S) are compared in Fig. 6. On the woven GDL, the MPL is not flat and the MPL thickness varies periodically according to the woven GDL substrate structure (Fig. 6a, tomographic images). On the carbon paper substrate, the MPL is flat, having negligible intrusion into the substrate. MPL on both substrate types have penetrating cracks.

The average total MPL porosity of W1S1009 and GDL 120S are 54% and 56%, respectively. The proximity of total porosity values is a result of consistent MPL microporosity (48% & 51%) and crack volume percentage (7.2% & 6.2%) of these two MPLs, despite on distinctly different types of substrates.

Local MPL porosity variations are observed for both MPLs, as visualized in the porosity maps in Fig. 6a and b. The MPL porosity heterogeneity (excluding of course the GDL-intruded regions) of W1S1009 and GDL 120S are 3.4 ± 0.9 and 2.3 ± 0.1 , respectively. It shows that on a bulk scale, the porosity variation, taking the cracks' density and distribution into account, is larger for woven-substrate-based W1S1009 than for GDL 120S based on a paper material.

3.3.2. Porosity profiles

The microporosity profiles and total porosity profiles of the CeTech materials are provided separately in Fig. 7.

The MPL microporosity profiles in Fig. 7a indicate that the woven GDLs (W1S1009 and W1S1010) have lower MPL microporosity than the carbon paper GDLs (GDL 120S and GDL 210S). Also, the woven GDLs' MPLs intrude deeper in the substrates.

Furthermore, the total porosity profiles of W1S1009 and W1S1010 (Fig. 7b) reveal a clear total porosity gradient in the GDL direction. This is caused by the intruding MPLs having noticeably lower porosity than the GDL substrates.

Also for the GDL 120S and GDL 210S, the decrease in porosity at the

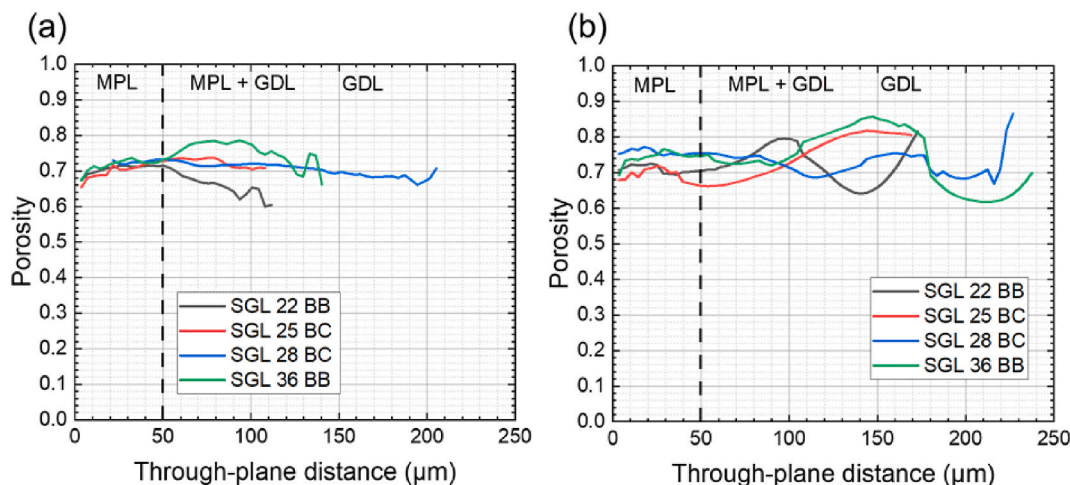


Fig. 5. Sigracet® materials' (a) MPL microporosity profiles and (b) in-plane average total porosity profiles.

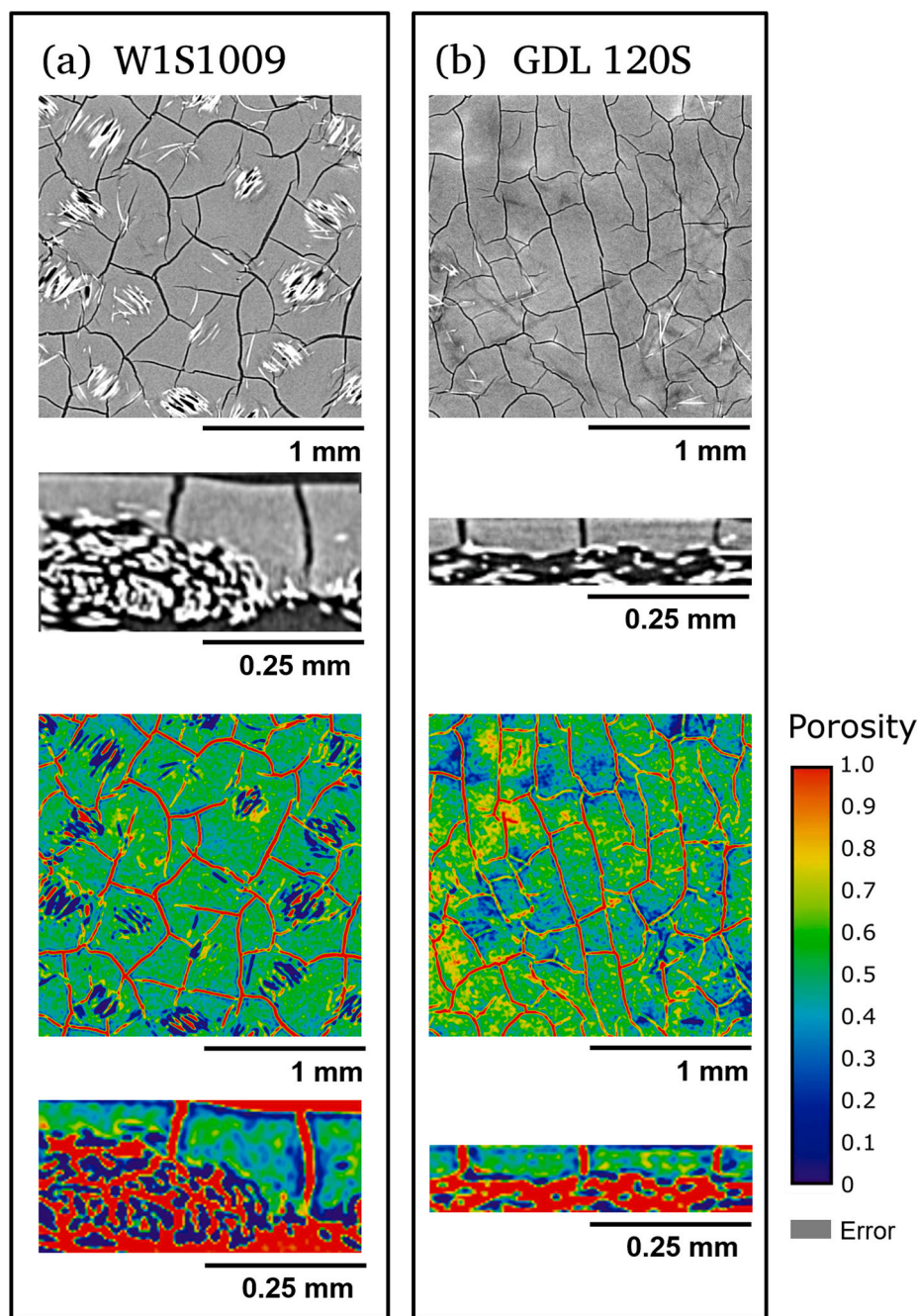


Fig. 6. Tomographic images and porosity maps of the MPLs of (a) W1S1009 and (b) GDL 120S; the error under the calibration bar denotes 1σ error for single-voxel porosity reading in the porosity maps.

MPL/GDL interfacial region is a result of lower MPL porosity and GDL fiber intrusion in the flat MPLs. A similar effect has been observed for H23 materials, where the MPLs are flat and have lower porosity than the GDL substrates. Due to different binder contents, the GDL 120S and GDL 210S also differ markedly in the substrate zone.

The total porosity, microporosity, thickness and porosity heterogeneity of the CeTech materials are summarized in Table 1.

4. Summary

MPLs from Freudenberg, Sigracet® and CeTech are distinguishably different in porosity. This leads to negligible, mild and noticeable porosity gradients toward the GDL substrate for Sigracet®, Freudenberg H23 and CeTech woven materials, respectively.

Although the thickness of MPL coatings can be adjusted freely during manufacturing processes and is independent of the substrate thickness, generally, thicker MPLs are still found to imply higher MPL volume ratios among the commercial materials. While the majority have MPL volume percentages $\leq 30\%$, the MPL volume percentage can be as low as 12% and as high as 45%. In the case of SGL 28 BC, the average MPL thickness exceeds 100 μm and reaches almost half of the total GDL volume (Fig. 8a).

Sorting by average MPL effective thickness versus total porosity, the scatter chart in Fig. 8b reaffirms the tendency of MPLs coming in groups by manufacturer due to comparable properties. It is likely a result of related slurry composition or sintering processes that are manufacturer-specific.

Furthermore, a positive correlation exists between the MPL effective

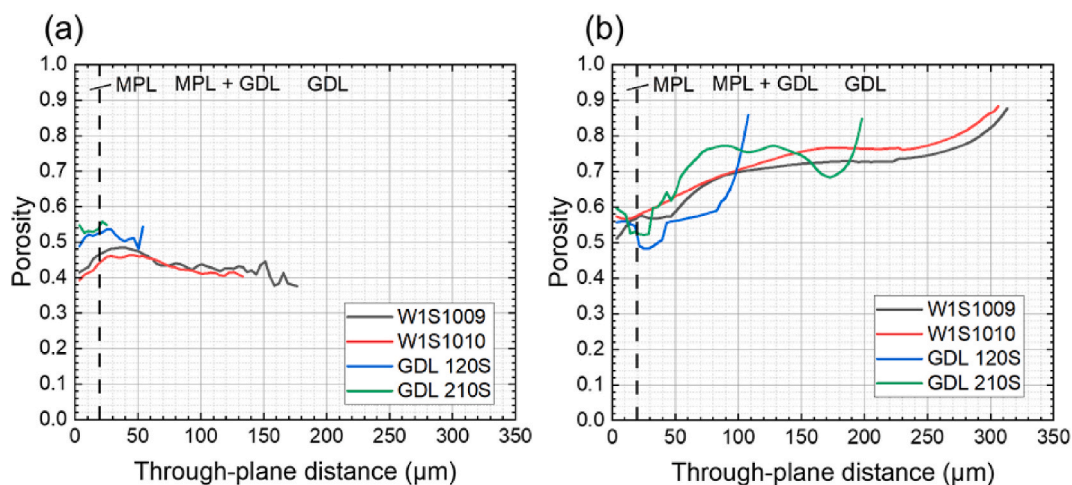


Fig. 7. CeTech materials' (a) MPL microporosity profiles and (b) in-plane average total porosity profiles.

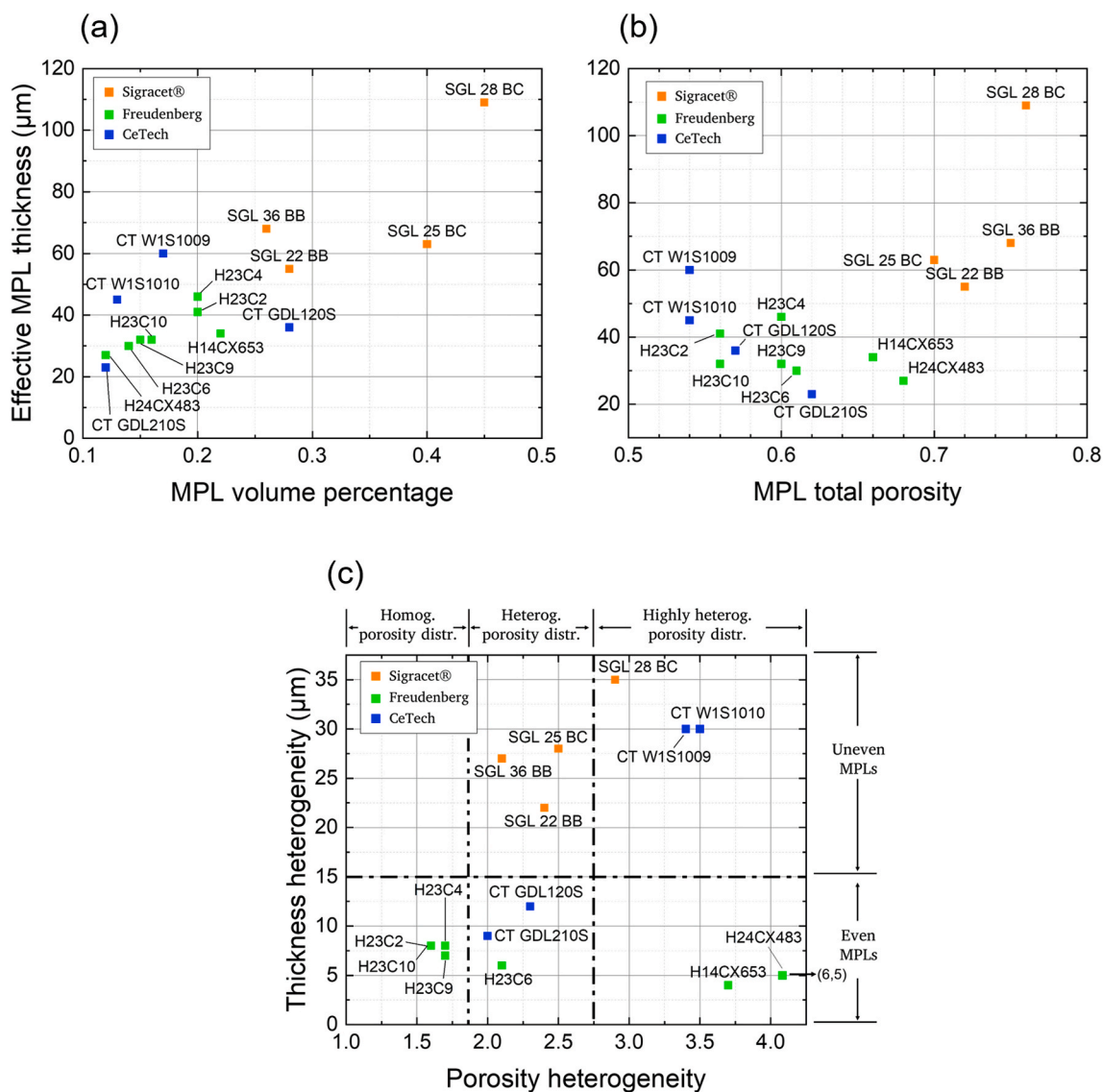


Fig. 8. Properties of gas diffusion layers sorted by (a) average effective MPL thickness vs. MPL volume percentage, (b) average effective MPL thickness vs. MPL total porosity and (c) MPL thickness heterogeneity vs. MPL porosity heterogeneity.

thickness and the porosity of the Sigracet® and Freudenberg materials. The high MPL porosity of Sigracet® materials, allowing higher effective diffusivity, may be a factor permitting the Sigracet® MPLs to be the thickest of all materials, without causing excessive hampering effects on gas diffusivity and consequently fuel cell performance.

Finally, based on the quantitative understanding of MPL porosity heterogeneity and thickness heterogeneity, the Freudenberg, Sigracet® and CeTech materials are categorized into two thickness heterogeneity groups (even and uneven MPLs; “even” means the local MPL thickness varies little across the MPL) and three porosity heterogeneity groups to stress the fact that, even among the heterogeneous porosity MPLs, some MPLs are still significantly more heterogeneous than others.

This categorization results in 5 groups of MPLs (Fig. 8c):

- Even MPLs with homogeneous porosity (distributions): H23C2, H23C4, H23C9 and H23C10 materials
- Even MPLs with heterogeneous porosity: H23C6, CT GDL 120S and CT GDL 210S
- Even MPLs with highly heterogeneous porosity: H14CX653 and H24CX483
- Uneven MPLs with heterogeneous porosity: SGL 22 BB, SGL 25 BC and SGL 36 BB
- Uneven MPLs with highly heterogeneous porosity: SGL 28 BC, W1S1009, W1S1010.

The categorization of the commercially available MPL types, classifying them into the five different groups, demonstrates the variability of today's commercial MPLs structures. Today, there is no fundamental understanding on how these structure characteristics influence fuel cell performance under different operating conditions. The present work supports future characterization of this structure-property relationship.

5. Conclusion

The morphology and porosity of MPLs on GDL substrates are important parameters for optimizing the water management and performance in fuel cells. Therefore, various types of microporous layer coatings of 15 commercially available GDLs from three major international manufacturers are analyzed for their morphology and porosity using X-ray tomographic microscopy on multi-millimeter sized samples. The size scale covers the important and highly relevant channel/rib scale in fuel cells. Additionally, the three-dimensional information from X-ray tomographic microscopy also enables the identification and quantification of MPL porosity variations on that scale, which is not possible with porosimetry or nanoscale imaging techniques.

CeTech materials' MPLs have generally the lowest total porosity and SGL materials have the highest among the 15 materials. The average total porosity difference between the least (CT W1 materials, 54%) and most porous MPLs (SGL 28 BC, 76%) reaches up to 22%, and it results in various degrees of porosity gradient from the MPL to GDL substrate.

The MPL local thickness of H23, CX and CT carbon paper materials remains similar in in-plane directions; these MPLs are considered even. On the contrary, SGL and CT W1 woven materials are highly uneven; strong MPL intrusion into the GDL substrate is commonly observed.

Furthermore, the MPL porosity heterogeneity is found to be a non-trivial property that describes MPL porosity variations caused by the cracks, holes and local density differences.

With the noticeable dissimilarity in evenness, thickness, porosity and porosity distribution, it is shown that homogeneous assumptions for MPLs do not always hold as they depend on the manufacturing processes and providers. MPLs should not be regarded as “smooth, thin layers” without inspection.

The results presented here may not yet provide a guideline on the use of these GDLs for specific PEFC operating conditions, because the two-phase flow and water transport in gas diffusion layers depend also on other factors, such as the pore size distribution, surface wettability and

thermal conductivity of both the MPL and the gas diffusion substrates. Nevertheless, the methodology here, based on frequently available CT scanner infrastructure, can help correlate the structure-function relationship of future MPL developments and PEFC performance characterization. The values and results presented here will also provide realistic input to PEFC modeling research and support the development and understanding of advanced MPL designs—such as gradient porosity and heterogeneous structures.

Funding

All the authors thankfully acknowledge funding from the Swiss National Science Foundation, under the funding scheme Sinergia (project grant number 180335).

CRediT authorship contribution statement

Yen-Chun Chen: Methodology, Validation, Writing – original draft. **Chrysoula Karageorgiou:** Experiments, Data acquisition and Curation. **Jens Eller:** Conceptualization. **Thomas J. Schmidt:** Supervision. **Felix N. Büchi:** Conceptualization, Supervision, Writing – review & editing.

Declaration of competing interest

The authors declare that they have no known competing financial interests or personal relationships that could have appeared to influence the work reported in this paper.

Acknowledgment

The authors would like to thank Tobias Schuler and Salvatore De Angelis (both PSI) for providing the sample holder for X-ray tomographic microscopy experiments. We acknowledge the help from Christoph Csoklich (PSI) for the assistance with the maintenance and operation of the laboratory computed tomography scanner. We appreciate the insightful discussions with Prof. Dr. Hubert Gasteiger and Anne Berger (TU Munich). The author Yen-Chun Chen would like to thank Hao-Wen Luo at National Tsing Hua University for discussions on discernability.

Appendix A. Supplementary data

Supplementary data to this article can be found online at <https://doi.org/10.1016/j.jpowsour.2022.231612>.

References

- [1] M.J. O'Malley, M.B. Anwar, S. Heinen, T. Kober, J. McCalley, M. McPherson, M. Muratori, A. Orths, M. Ruth, T.J. Schmidt, A. Tuohy, Multicarrier energy systems: shaping our energy future, *Proc. IEEE* 108 (9) (2020) 1437–1456, <https://doi.org/10.1109/JPROC.2020.2992251>.
- [2] Y. Nagai, J. Eller, T. Hatanaka, S. Yamaguchi, S. Kato, A. Kato, F. Marone, H. Xu, F. N. Büchi, Improving water management in fuel cells through microporous layer modifications: fast operando tomographic imaging of liquid water, *J. Power Sources* 435 (March) (2019) 226809, <https://doi.org/10.1016/j.jpowsour.2019.226809>, 226809.
- [3] W. Yoshimune, S. Kato, S. Yamaguchi, Y. Akimoto, A. Koiwai, H. Nakamura, Managing the pore morphologies of microporous layers for polymer electrolyte fuel cells with a solvent-free coating technique, *ACS Sustain. Chem. Eng.* 9 (23) (2021) 7922–7929, <https://doi.org/10.1021/acssuschemeng.1c02105>.
- [4] M.F. Mathias, J. Roth, J. Fleming, W. Lehnert, Diffusion media materials and characterisation, in: W. Vielstich, A. Lamm, H.A. Gasteiger, H. Yokokawa (Eds.), *Handbook of Fuel Cells*, John Wiley & Sons, Ltd, Chichester, UK, 2010, p. f303046, <https://doi.org/10.1002/9780470974001.f303046>.
- [5] J. Zhou, S. Shukla, A. Putz, M. Secanell, Analysis of the role of the microporous layer in improving polymer electrolyte fuel cell performance, *Electrochim. Acta* 268 (2018) 366–382, <https://doi.org/10.1016/j.electacta.2018.02.100>.
- [6] H. Liu, M.G. George, R. Zeis, M. Messerschmidt, J. Scholta, A. Bazylak, The impacts of microporous layer degradation on liquid water distributions in polymer electrolyte membrane fuel cells using synchrotron imaging, *ECS Trans* 80 (8) (2017) 155–164, <https://doi.org/10.1149/08008.0155sest>.

- [7] N. Holmström, J. Ihonen, A. Lundblad, G. Lindbergh, The influence of the gas diffusion layer on water management in polymer electrolyte fuel cells, *Fuel Cell* 7 (4) (2007) 306–313, <https://doi.org/10.1002/fuce.200700003>.
- [8] Z. Qi, A. Kaufman, Improvement of water management by a microporous sublayer for PEM fuel cells, *J. Power Sources* 109 (1) (2002) 38–46, [https://doi.org/10.1016/S0378-7753\(02\)00058-7](https://doi.org/10.1016/S0378-7753(02)00058-7).
- [9] H.K. Atiyeh, E. Halliop, J. Pharoah, K. Karan, A. Phoenix, B. Peppley, Experimental investigation of the role of a microporous layer on the water transport and performance of a PEM fuel cell, *J. Power Sources* 170 (1) (2007) 111–121, <https://doi.org/10.1016/j.jpowsour.2007.04.016>.
- [10] J. Chen, T. Matsuura, M. Hori, Novel gas diffusion layer with water management function for PEMFC, *J. Power Sources* 131 (1–2) (2004) 155–161, <https://doi.org/10.1016/j.jpowsour.2004.01.007>.
- [11] R. Lin, L. Chen, T. Zheng, S. Tang, X. Yu, M. Dong, Z. Hao, Interfacial water management of gradient microporous layer for self-humidifying proton exchange membrane fuel cells, *Int. J. Heat Mass Tran.* 175 (2021) 121340, <https://doi.org/10.1016/j.ijheatmasstransfer.2021.121340>.
- [12] J.H. Nam, K.-J. Lee, G.-S. Hwang, C.-J. Kim, M. Kaviany, Microporous layer for water morphology control in PEMFC, *Int. J. Heat Mass Tran.* 52 (11–12) (2009) 2779–2791, <https://doi.org/10.1016/j.ijheatmasstransfer.2009.01.002>.
- [13] J.H. Nam, M. Kaviany, Effective diffusivity and water-saturation distribution in single- and two-layer PEMFC diffusion medium, *Int. J. Heat Mass Tran.* 46 (24) (2003) 4595–4611, [https://doi.org/10.1016/S0017-9310\(03\)00305-3](https://doi.org/10.1016/S0017-9310(03)00305-3).
- [14] J.P. Owejan, J.E. Owejan, W. Gu, T.A. Trabold, T.W. Tighe, M.F. Mathias, Water transport mechanisms in PEMFC gas diffusion layers, *J. Electrochem. Soc.* 157 (10) (2010) B1456, <https://doi.org/10.1149/1.3468615>.
- [15] Y. Tabe, Y. Aoyama, K. Kadowaki, K. Suzuki, T. Chikahisa, Impact of micro-porous layer on liquid water distribution at the catalyst layer interface and cell performance in a polymer electrolyte membrane fuel cell, *J. Power Sources* 287 (2015) 422–430, <https://doi.org/10.1016/j.jpowsour.2015.04.095>.
- [16] G. Lin, T.V. Nguyen, A two-dimensional two-phase model of a PEM fuel cell, *J. Electrochem. Soc.* 153 (2) (2006) A372, <https://doi.org/10.1149/1.2142267>.
- [17] P. Deevanhay, T. Sasabe, S. Tsushima, S. Hirai, Effect of liquid water distribution in gas diffusion media with and without microporous layer on PEM fuel cell performance, *Electrochem. Commun.* 34 (2013) 239–241, <https://doi.org/10.1016/j.elecom.2013.07.001>.
- [18] Z. Lu, M.M. Daino, C. Rath, S.G. Kandlikar, Water management studies in PEM fuel cells, Part III: dynamic breakthrough and intermittent drainage characteristics from GDIs with and without MPLs, *Int. J. Hydrogen Energy* 35 (9) (2010) 4222–4233, <https://doi.org/10.1016/j.ijhydene.2010.01.012>.
- [19] J.T. Gostick, M.A. Ioannidis, M.W. Fowler, M.D. Pritzker, On the role of the microporous layer in PEMFC operation, *Electrochem. Commun.* 11 (3) (2009) 576–579, <https://doi.org/10.1016/j.elecom.2008.12.053>.
- [20] A.Z. Weber, J. Newman, Effects of microporous layers in polymer electrolyte fuel cells, *J. Electrochem. Soc.* 152 (4) (2005) A677, <https://doi.org/10.1149/1.1861194>.
- [21] U. Pasaogullari, C.-Y. Wang, K.S. Chen, Two-phase transport in polymer electrolyte fuel cells with bilayer cathode gas diffusion media, *J. Electrochem. Soc.* 152 (8) (2005) A1574, <https://doi.org/10.1149/1.1938067>.
- [22] D. Spornjak, A.K. Prasad, S.G. Advani, Experimental investigation of liquid water formation and transport in a transparent single-serpentine PEM fuel cell, *J. Power Sources* 170 (2) (2007) 334–344, <https://doi.org/10.1016/j.jpowsour.2007.04.020>.
- [23] X. Wang, T.V. Nguyen, Modeling the effects of the cathode micro-porous layer on the performance of a PEM fuel cell, *ECS Trans* 16 (2) (2019) 3–12, <https://doi.org/10.1149/1.2981838>.
- [24] H. Naito, K. Ishikawa, T. Sasabe, S. Hirai, T. Tanuma, Investigation of effects of hydrophilic micro-porous layer on liquid water behavior by X-ray imaging, *J. Power Sources* 507 (2021) 230285, <https://doi.org/10.1016/j.jpowsour.2021.230285>.
- [25] Y. Aoyama, K. Suzuki, Y. Tabe, T. Chikahisa, T. Tanuma, Water transport and PEFC performance with different interface structure between micro-porous layer and catalyst layer, *J. Electrochem. Soc.* 163 (5) (2016) F359–F366, <https://doi.org/10.1149/2.0451605jes>.
- [26] C. Simon, J. Endres, B. Nefzger-Loders, F. Wilhelm, H.A. Gasteiger, Interaction of pore size and hydrophobicity/hydrophilicity for improved oxygen and water transport through microporous layers, *J. Electrochem. Soc.* 14 (2019).
- [27] M.N. Islam, U. Shrivastava, M. Atwa, X. Li, V. Birss, K. Karan, Highly ordered nanoporous carbon scaffold with controllable wettability as the microporous layer for fuel cells, *ACS Appl. Mater. Interfaces* 12 (35) (2020) 39215–39226, <https://doi.org/10.1021/acsami.0c10755>.
- [28] C. Simon, D. Kartouzian, D. Müller, F. Wilhelm, H.A. Gasteiger, Impact of microporous layer pore properties on liquid water transport in PEM fuel cells: carbon black type and perforation, *J. Electrochem. Soc.* 164 (14) (2017) F1697–F1711, <https://doi.org/10.1149/2.1321714jes>.
- [29] T. Tanuma, M. Kawamoto, S. Kinoshita, Effect of properties of hydrophilic microporous layer (MPL) on PEFC performance, *J. Electrochem. Soc.* 164 (6) (2017) F499–F503, <https://doi.org/10.1149/2.0371706jes>.
- [30] R.W. Atkinson, Y. Garsany, B.D. Gould, K.E. Swider-Lyons, I.V. Zenyuk, The role of compressive stress on gas diffusion media morphology and fuel cell performance, *ACS Appl. Energy Mater.* 1 (1) (2017) 191–201, <https://doi.org/10.1021/acsaem.7b00077>.
- [31] S.G. Kandlikar, M.L. Garofalo, Z. Lu, Water management in a PEMFC: water transport mechanism and material degradation in gas diffusion layers, *Fuel Cell* 6 (2011) 814–823, <https://doi.org/10.1002/fuce.201000172>.
- [32] S. Hasanpour, M. Hoorfar, A.B. Phillion, Characterization of transport phenomena in porous transport layers using X-ray microtomography, *J. Power Sources* 353 (2017) 221–229, <https://doi.org/10.1016/j.jpowsour.2017.03.153>.
- [33] T. Sasabe, P. Deevanhay, S. Tsushima, S. Hirai, Soft X-ray visualization of the liquid water transport within the cracks of micro porous layer in PEMFC, *Electrochem. Commun.* 13 (6) (2011) 638–641, <https://doi.org/10.1016/j.elecom.2011.03.033>.
- [34] X. Zhang, Y. Gao, H. Ostadi, K. Jiang, R. Chen, Modelling water intrusion and oxygen diffusion in a reconstructed microporous layer of PEM fuel cells, *Int. J. Hydrogen Energy* 39 (30) (2014) 17222–17230, <https://doi.org/10.1016/j.ijhydene.2014.08.027>.
- [35] J.H. Chun, D.H. Jo, S.G. Kim, S.H. Park, C.H. Lee, S.H. Kim, Improvement of the mechanical durability of micro porous layer in a proton exchange membrane fuel cell by elimination of surface cracks, *Renew. Energy* 48 (2012) 35–41, <https://doi.org/10.1016/j.renene.2012.04.011>.
- [36] M. Wang, S. Medina, J.R. Pfeilsticker, S. Pylypenko, M. Ulsh, S.A. Mauger, Impact of microporous layer roughness on gas-diffusion-electrode-based polymer electrolyte membrane fuel cell performance, *ACS Appl. Energy Mater.* 2 (11) (2019) 7757–7761, <https://doi.org/10.1021/acsaem.9b01871>.
- [37] J. Shi, Z. Zhan, D. Zhang, Y. Yu, X. Yang, L. He, M. Pan, Effects of cracks on the mass transfer of polymer electrolyte membrane fuel cell with high performance membrane electrode assembly, *J. Wuhan Univ. Technol.-Materials Sci. Ed.* 36 (3) (2021) 318–330, <https://doi.org/10.1007/s11595-021-2412-z>.
- [38] S.S. Alrwashdeh, H. Markötter, J. Haußmann, T. Arlt, M. Klages, J. Scholta, J. Banhart, I. Manke, Investigation of water transport dynamics in polymer electrolyte membrane fuel cells based on high porous micro porous layers, *Energy* 102 (2016) 161–165, <https://doi.org/10.1016/j.energy.2016.02.075>.
- [39] Y. Aoyama, K. Suzuki, Y. Tabe, T. Chikahisa, Observation of water transport in the micro-porous layer of a polymer electrolyte fuel cell with a freezing method and cryo-scanning electron microscope, *Electrochem. Commun.* 41 (2014) 72–75, <https://doi.org/10.1016/j.elecom.2013.12.029>.
- [40] F. Akitomo, T. Sasabe, T. Yoshida, H. Naito, K. Kawamura, S. Hirai, Investigation of effects of high temperature and pressure on a polymer electrolyte fuel cell with polarization analysis and X-ray imaging of liquid water, *J. Power Sources* 431 (April) (2019) 205–209, <https://doi.org/10.1016/j.jpowsour.2019.04.115>.
- [41] J. Roth, J. Eller, F. Marone, F.N. Büchi, Investigation of the representative area of the water saturation in gas diffusion layers of polymer electrolyte fuel cells, *J. Phys. Chem. C* 117 (49) (2013) 25991–25999, <https://doi.org/10.1021/jp4057169>.
- [42] J.T. Gostick, M.W. Fowler, M.A. Ioannidis, M.D. Pritzker, Y.M. Volfkovich, A. Sakars, Capillary pressure and hydrophilic porosity in gas diffusion layers for polymer electrolyte fuel cells, *J. Power Sources* 156 (2) (2006) 375–387, <https://doi.org/10.1016/j.jpowsour.2005.05.086>.
- [43] C.S. Kong, D.-Y. Kim, H.-K. Lee, Y.-G. Shul, T.-H. Lee, Influence of pore-size distribution of diffusion layer on mass-transport problems of proton exchange membrane fuel cells, *J. Power Sources* 7 (2002).
- [44] Jordan, L. R.; Shukla, A. K.; Behrsing, T.; Avery, N. R.; Muddle, B. C.; Forsyth, M. Effect of Diffusion-Layer Morphology on the Performance of Polymer Electrolyte Fuel Cells Operating at Atmospheric Pressure. vol. 6.
- [45] E. Antolini, A. Pozio, L. Giorgi, E. Antolini, Morphological characteristics of carbon/polytetrafluoroethylene films deposited on porous carbon support, *J. Mater. Sci.* 33 (7) (1998) 1837–1843, <https://doi.org/10.1023/A:1004349103997>.
- [46] J. Ma, X. Zhang, Z. Jiang, H. Ostadi, K. Jiang, R. Chen, Flow properties of an intact MPL from nano-tomography and pore network modelling, *Fuel* 136 (2014) 307–315, <https://doi.org/10.1016/j.fuel.2014.07.040>.
- [47] M. Göbel, M. Godehardt, K. Schladitz, Multi-scale structural analysis of gas diffusion layers, *J. Power Sources* 355 (2017) 8–17, <https://doi.org/10.1016/j.jpowsour.2017.03.086>.
- [48] E.A. Wargo, V.P. Schulz, A. Çeçen, S.R. Kalidindi, E.C. Kumbur, Resolving macro- and micro-porous layer interaction in polymer electrolyte fuel cells using focused ion beam and X-ray computed tomography, *Electrochim. Acta* 87 (2013) 201–212, <https://doi.org/10.1016/j.electacta.2012.09.008>.
- [49] S.S. Alrwashdeh, I. Manke, H. Marko, M. Klages, M. Go, In operando quantification of three-dimensional water distribution in nanoporous carbon-based layers in polymer electrolyte membrane fuel cells, <https://doi.org/10.1021/acsnano.7b01720>, 2017.
- [50] R. Banerjee, J. Hinebaugh, H. Liu, R. Yip, N. Ge, A. Bazylak, Heterogeneous porosity distributions of polymer electrolyte membrane fuel cell gas diffusion layer materials with rib-channel compression, *Int. J. Hydrogen Energy* 41 (33) (2016) 14885–14896, <https://doi.org/10.1016/j.ijhydene.2016.06.147>.
- [51] D. Muirhead, R. Banerjee, J. Lee, M.G. George, N. Ge, H. Liu, S. Chevalier, J. Hinebaugh, K. Han, A. Bazylak, Simultaneous characterization of oxygen transport resistance and spatially resolved liquid water saturation at high-current density of polymer electrolyte membrane fuel cells with varied cathode relative humidity, *Int. J. Hydrogen Energy* 42 (49) (2017) 29472–29483, <https://doi.org/10.1016/j.ijhydene.2017.10.031>.
- [52] Q. Meyer, S. Ashton, P. Boillat, M. Cochet, E. Engebretsen, D.P. Finegan, X. Lu, J. Bailey, N. Mansor, R. Abdulaziz, O.O. Taiwo, R. Jervis, S. Torija, P. Benson, S. Foster, P. Adcock, P.R. Shearing, D.J.L. Brett, Effect of gas diffusion layer properties on water distribution across air-cooled, open-cathode polymer electrolyte fuel cells: a combined ex-situ X-ray tomography and in-operando neutron imaging study, *Electrochim. Acta* 211 (2016) 478–487, <https://doi.org/10.1016/j.electacta.2016.06.068>.

- [53] H. Tang, S. Wang, M. Pan, R. Yuan, Porosity-graded micro-porous layers for polymer electrolyte membrane fuel cells, *J. Power Sources* 166 (1) (2007) 41–46, <https://doi.org/10.1016/j.jpowsour.2007.01.021>.
- [54] L. Chen, R. Lin, S. Tang, D. Zhong, Z. Hao, Structural design of gas diffusion layer for proton exchange membrane fuel cell at varying humidification, *J. Power Sources* 467 (2020) 228355, <https://doi.org/10.1016/j.jpowsour.2020.228355>.
- [55] A. Mohseninia, D. Kartouzian, R. Schlumberger, H. Markötter, F. Wilhelm, J. Scholta, I. Manke, Enhanced water management in PEMFCs: perforated catalyst layer and microporous layers, *ChemSusChem* 13 (11) (2020) 2931–2934, <https://doi.org/10.1002/cssc.202000542>.
- [56] Y.-C. Chen, A. Berger, S. De Angelis, T. Schuler, M. Bozzetti, J. Eller, V. Tileli, T. J. Schmidt, F.N. Büchi, A method for spatial quantification of water in microporous layers of polymer electrolyte fuel cells by X-ray tomographic microscopy, *ACS Appl. Mater. Interfaces* 13 (14) (2021) 16227–16237, <https://doi.org/10.1021/acsami.0c22358>.
- [57] Chantler, C. T. Theoretical form factor, attenuation, and scattering tabulation for $Z=1-92$ from $E=1-10$ EV to $E=0.4-1.0$ MeV. *J. Phys. Chem. Ref. Data* 24 71 1995 1995, 24 (1), 71.
- [58] C.T. Chantler, Detailed tabulation of atomic form factors, photoelectric absorption and scattering cross section, and mass attenuation coefficients in the vicinity of absorption edges in the soft X-ray ($Z=30-36$, $Z=60-89$, $E=0.1$ KeV–10 KeV), addressing convergence issues, *J. Phys. Chem. Ref. Data* 29 (4) (2000) 597, <https://doi.org/10.1107/S0909049501008305>.
- [59] A. Fedorov, R. Beichel, J. Kalpathy-Cramer, J. Finet, J.-C. Fillion-Robin, S. Pujol, C. Bauer, D. Jennings, F. Fennessy, M. Sonka, J. Buatti, S.R. Aylward, J.V. Miller, S. Pieper, R. Kikinis, 3D slicer as an image computing platform for the quantitative imaging network, *Magn. Reson. Imaging* Nov 30 (9) (2012) 1323–1341.
- [60] A. El-kharouf, T.J. Mason, D.J.L. Brett, B.G. Pollet, Ex-situ characterisation of gas diffusion layers for proton exchange membrane fuel cells, *J. Power Sources* 218 (2012) 393–404, <https://doi.org/10.1016/j.jpowsour.2012.06.099>.